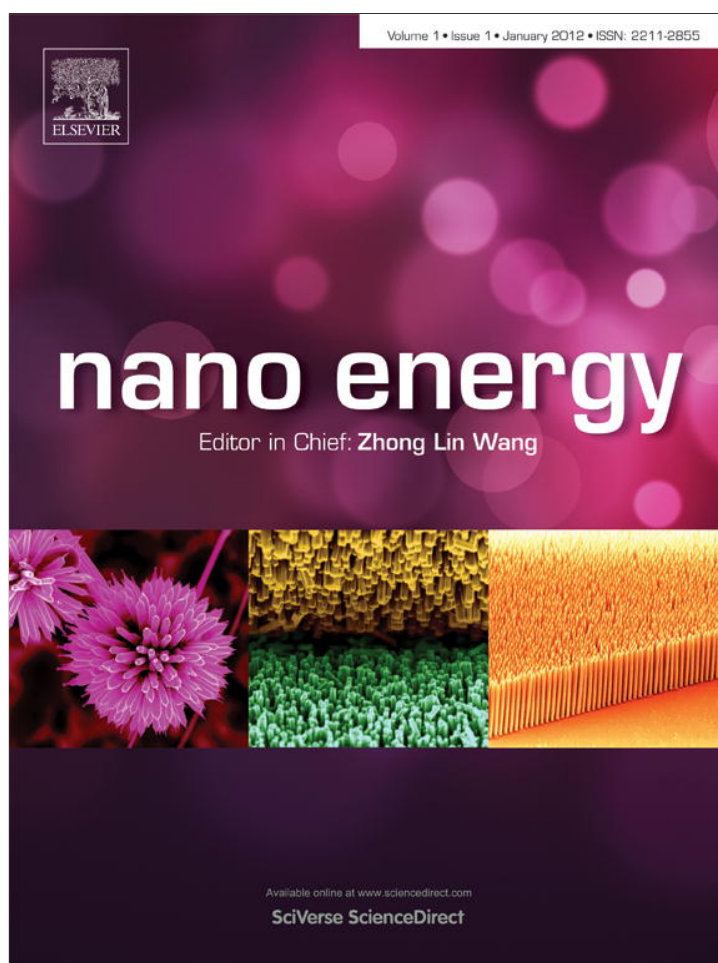


Provided for non-commercial research and education use.
Not for reproduction, distribution or commercial use.

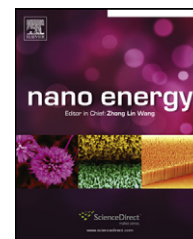


This article appeared in a journal published by Elsevier. The attached copy is furnished to the author for internal non-commercial research and education use, including for instruction at the authors institution and sharing with colleagues.

Other uses, including reproduction and distribution, or selling or licensing copies, or posting to personal, institutional or third party websites are prohibited.

In most cases authors are permitted to post their version of the article (e.g. in Word or Tex form) to their personal website or institutional repository. Authors requiring further information regarding Elsevier's archiving and manuscript policies are encouraged to visit:

<http://www.elsevier.com/copyright>

Available online at www.sciencedirect.com**SciVerse ScienceDirect**journal homepage: www.elsevier.com/locate/nanoenergy

REVIEW

Piezoelectric nanogenerators—Harvesting ambient mechanical energy at the nanometer scale

Xudong Wang

Department of Materials Science and Engineering, University of Wisconsin-Madison, WI 53706, USA

Received 19 August 2011; received in revised form 16 September 2011; accepted 16 September 2011

Available online 4 October 2011

KEYWORDSNanogenerator;
Piezoelectric;
ZnO;
Mechanical energy
harvesting;
Nanowire**Abstract**

Harvesting ambient mechanical energy at the nanometer scale holds great promises for powering small electronics and achieving self-powered electronic devices. The self-powering capability allows electronic device packages to exclude bulky energy storage components and makes possible forgoing the inclusion of bulky battery components. Recent development of nanogenerators (NGs) has demonstrated a possible solution for the design of self-sufficient power source that directly draws energy from ambient mechanical resources. Piezoelectric nanowires (NWs) are the building blocks of NGs. In this review paper, theoretical calculations and experimental characterization methods for predicting or determining the piezoelectric potential output of NWs are reviewed first. Representative models of NGs are then discussed for harvesting mechanical energy from high-frequency acoustic waves and low-frequency vibrations/frictions. A numerical calculation is also presented to estimate the energy output from NW-based NGs. A potential practical application of NGs for harvesting energy from respiration is shown using piezoelectric polymer thin films. At the end, perspectives of the NG concept are discussed. The nanometer-scale piezoelectric and mechanical properties, the piezotronic effect, and large-scale manufacturing capability are suggested to be the essential aspects that would eventually lead the promising NG concept to a practical power source. © 2011 Elsevier Ltd. All rights reserved.

Introduction

Vibration-based mechanical energy is the most ubiquitous and accessible energy source in the surroundings. For random vibrations with frequencies from hundreds Hz to kHz, the available energy density is within the range of a few hundred microwatt to milliwatts per cubic centimeter [1,2]. Therefore, harvesting this type of energy offers a great

potential for remote/wireless sensing, charging batteries, and powering electronic devices [3-8].

Devices to harvest the vibration-based energy have been successfully built on three different principles: piezoelectric [9], electrostatic [10], and electromagnetic [11] transducers in micro-electromechanical systems (MEMS). Among these techniques, piezoelectric transducer is distinguished by its high practical output power and relatively easier manufacturing. The designs are mostly based on the cantilever beam configuration and a single operational unit is typically in the size range from hundreds of micrometers to centimeters.

E-mail address: xudong@engr.wisc.edu

The relatively large size and the ceramic-thin-film-based functional unit may restrict its compatibility to nano- or micro-electronic systems and further improvement of the power density.

In addition, with the rapid development of nanotechnology, solar, thermal, and chemical energy harvesting technologies are experiencing a magnificent improvement on their building blocks, designs, efficiencies, as well as costs. Therefore, although the merits of scavenging ambient mechanical energy are unique, whether this technique can compete for entry into the mainstream of the renewable/alternative energy field would largely rely on the creation and development of new materials, new designs, and even new principles that may take the advantage of nanotechnology in shrinking the size and improving the performance [12,13].

Recently, piezoelectric ZnO nanowires (NWs) have been demonstrated as a promising concept to harvest micro- and nano-scale mechanical energy from the surrounding—the *nanogenerator* (NG) [14]. This device has the potential to fundamentally improve the mechanical energy harvesting capability with advanced NW building blocks and compact designs, which might eventually lead to an effective power source for self-powered electronic systems with higher energy density, higher efficiency, longer life time, as well as lower cost [15–17]. In this review article, the fundamental operation principles, energy harvesting capabilities, and practical designs of piezoelectric NGs will be reviewed and the perspective of this novel technique will be discussed.

Piezoelectric NWs for mechanical energy harvesting

NW is a one dimensional (1D) nanomaterial that typically has a diameter less than 100 nm and a length more than 1 μm . Most ceramic NWs are single crystals. Compared to the conventional thin-film-based piezoelectric cantilever transducers, using piezoelectric NWs for mechanical energy scavenging offers three unique advantages:

- (1) *Enhanced piezoelectric effect.* 400–500% enhancement of the piezoelectric effect was predicted due to the flexoelectric effect [18], when a strain gradient is experienced by a ferroelectric NW with a thickness of a few tens of nanometers.

- (2) *Superior mechanical properties.* The lattice perfection of NWs enables much larger critical strain, higher flexibility, and longer operational lifetime.
- (3) *High sensitivity to small forces.* Large aspect ratio and small thickness allow the creation of significant strain in the NWs under a force at the nano-Newton or even pico-Newton level.

Herein, we will first review and discuss the theoretically predicted potential-strain relationship and the flexoelectric enhancement effect that are essential for predicting and evaluating the potential of a piezoelectric NW for mechanical energy harvesting. The experimental characterization of the piezoelectric output on different piezoelectric materials will also be reviewed.

Theoretical predictions

When a piezoelectric NW is deflected, a piezoelectric potential can be generated on the side surfaces due to the crystal lattice distortion. For ZnO NWs, the tensile side surface gives a positive potential; while a negative potential appears on the compressive side surface. In 2007, Gao and Wang did a theoretical calculation on the potential distribution in an ideal ZnO NW, which is a dielectric material without free charge carriers and subjecting no body force [19]. Perturbation expansion was applied to solve the potential distribution by assuming the NW has a cylindrical shape with a uniform cross-section. Calculation showed that the piezoelectric potential in the NW is independent on the length position. Thus, the NW would act approximately like a “parallel plate capacitor” (Fig. 1a). The calculated electric field distribution on the NW cross-section is shown in Fig. 1b, where the highest potential of $\sim \pm 0.27$ can be identified. This NW has a diameter of 50 nm and a length of 600 nm, and is bent 145 nm laterally at the tip by an 80 nN lateral force. The numerical calculation showed that the maximum piezoelectric potential that can be generated at the NW surface is directly proportional to the lateral displacement of the NW and inversely proportional to the length-to-diameter aspect ratio of the NW.

It should be noted that the above calculation was based on the assumption that there is no free charge carrier inside the ZnO NW. In such a case, ZnO was considered as a perfect insulating piezoelectric material. In reality, ZnO is a wide-bandgap semiconductor material and has considerably

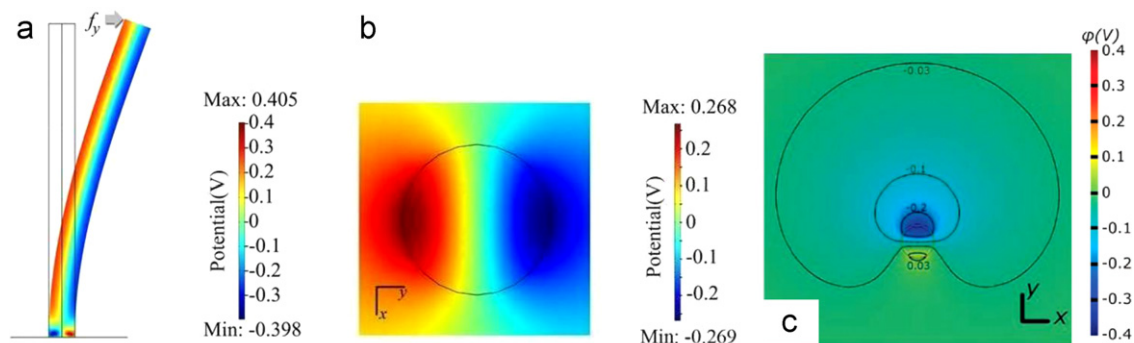


Figure 1 Potential distribution for a ZnO NW. (a) Side view of the potential profile. (b) Cross-sectional view of the piezoelectric potential [19]. (c) Cross-sectional view of the piezoelectric potential when the contribution of free electrons is considered [20].

amount of intrinsic defects that makes it n -type with a typical dopant concentration at the level of 10^{17} cm^{-3} . Thus, the free charge carrier effect needs to be considered for predicting the piezoelectric potential output.

Fig. 1c shows the overall potential distribution on a cross section perpendicular to the NW axis when the free charge contribution to the piezoelectric potential is considered [20]. This calculation was done by using the same ZnO constants as those used in the non-free-charge calculation and by selecting a typical doping concentration of $1 \times 10^{17} \text{ cm}^{-3}$. The electric potential maximum in the positive side of the NW is significantly reduced from $\sim 0.3 \text{ V}$ in Fig. 1b, which corresponds to an insulator case, to less than 0.05 V in Fig. 1c, which considers the moderate doping in ZnO. The potential on the negative potential side is very well preserved. The significant potential quenching at the positive side is due to the transportation of free electrons from substrate to the positive potential region. The negative potential side only interacts with the positively charged ionized donors. Therefore, at very high doping level, i.e. $> 10^{18} \text{ cm}^{-3}$, the negative potential side could be completely screened and the overall NW would exhibit no net potential output.

A comprehensive calculation was also presented to reveal the size-force-potential relationship for different piezoelectric nanomaterial morphologies [21]. By assuming the NWs are

uniform cantilever beams, numerical analysis was applied to ZnO and BaTiO₃. BaTiO₃ is a perovskite materials and ideally has a rectangular cross-section (Fig. 2a), which would produce uniform potential on the two side surfaces. ZnO has a hexagonal cross-section (Fig. 2b) and the piezoelectric potential was estimated on the two opposite planes of the hexagon. Thus, the maximum piezoelectric potential of rectangular and hexagonal NWs can be expressed by Eqs. (1) and (2), respectively:

$$\Delta V_{\max,rNW} = \frac{f_y(1+\nu)b^3e_{15}}{6I_{xx}[2(1+\nu)e_{15}^2+k_{11}E]} \quad (1)$$

$$\Delta V_{\max,hNW} = \frac{\sqrt{3}f_y(19+16\nu)b^3e_{15}}{36I_{xx}[2(1+\nu)e_{15}^2+k_{11}E]} \quad (2)$$

Above equations were used to estimate the potential-to-force relations of NWs when they are deflected under a constant external force (f_y). Both ZnO and BaTiO₃ in this analysis were considered as a perfect dielectric medium with negligible free charge carrier density. The maximum piezoelectric potentials were plotted as functions of the external force and their dimensions, as shown in the insets of Fig. 2c and d for BaTiO₃ and ZnO NWs, respectively. In general, their maximum potential is proportional to the

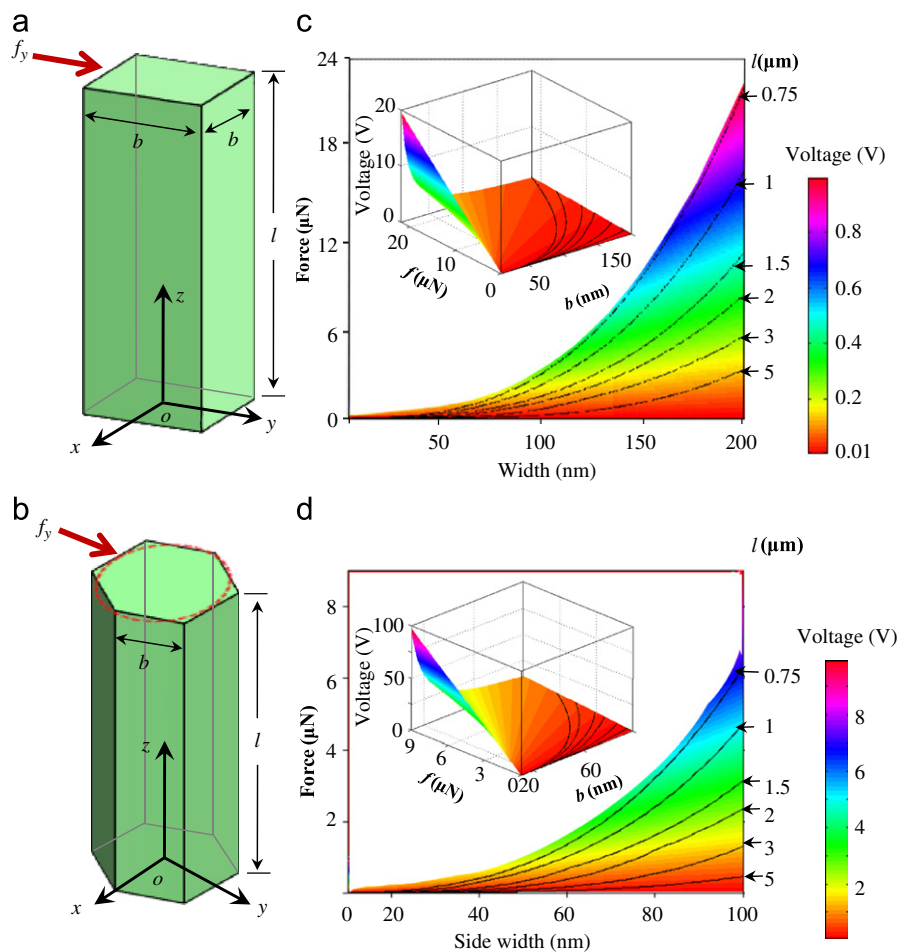


Figure 2 Schematic structures and the coordinate systems of (a) a rectangular NW and (b) a hexagonal NW. The static analysis of the maximum allowable piezoelectric potential that can be generated by (c) a BaTiO₃ NW and (d) a ZnO NW. Insets are the corresponding full range plots of the piezoelectric potential to the force and size relationships [21].

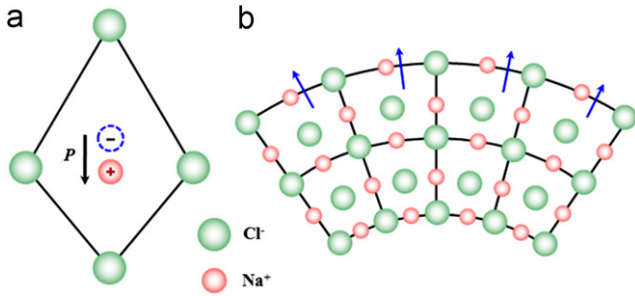


Figure 3 (a) Schematic of a NaCl unit cell under non-uniform strain. (b) Polarization in NaCl crystal due to bending.

external force and inversely proportional to the thickness or width but not related to their length. In real cases, the deflection of nanostructures is restricted by their mechanical strength and flexibility, thus the highest potentials plotted in the insets of Fig. 3c and d are practically impossible. In order to reveal the achievable piezoelectric potentials by NWs, the mechanical limitation boundaries were calculated and superimposed into the potential plots.

Thus, the mechanical limitation boundaries (dark lines in the insets of Fig. 3c and d) were calculated at 7.0% strain (from reported data on ZnO NWs [22]) and $\pm 30^\circ$ deflection angle, whichever was reached first. The boundary lines for NWs with various lengths were determined and the allowable potential distributions inside the boundary lines are shown in Fig. 2c and d for NWs with lengths of 0.75 μm , 1 μm , 1.5 μm , 2 μm , 3 μm , and 5 μm .

Comparing BaTiO₃ and ZnO NWs with the same size and under the same force, ZnO exhibits much higher piezoelectric potential, although its piezoelectric coefficient is much smaller than that of BaTiO₃. The reason for BaTiO₃ NWs to show lower potential is attributed to their much larger dielectric constant, which leads to a large capacitance. It is known that the piezoelectric effect directly induces charge and the piezoelectric potential is derived from the amount of charge via the relation $V=Q/C_p$. Therefore, significantly larger dielectric constant of BaTiO₃ would induce a lower effective voltage appearing along the NW surface.

Flexoelectric enhancement at the nanometer scale

When a NW is applied for mechanical energy harvesting, the NWs are acting as cantilevered beams with their one end fixed on the substrate and the other end free-standing. Thus, the piezoelectricity is generated by the bending induced lattice distortion rather than the uniform compression/extension along one axis. Under this circumstance, one important effect has to be considered is the flexoelectric effect [23,24], which is the polarization induced by inhomogeneous strain and is defined by the relation [25]

$$P_i = f_{ijkl} \frac{\partial \epsilon_{jk}}{\partial x_l} \quad (3)$$

where f_{ijkl} is the fourth rank tensor (or flexoelectric coefficient), P_i is the polarization, ϵ_{jk} is the elastic strain, and x_l is the direction of the strain gradient. The flexoelectricity is a more general property than piezoelectricity since a nonuniform lattice deformation could induce a charge displacement even in centrosymmetric systems [26,27], liquid crystals [28], soft

elastomers [29], and even biological species [30]. Fig. 3a illustrates a net dipole moment resulted from an inhomogeneous strain in a NaCl crystal. Once a strain gradient appears due to bending of the crystal, flexoelectricity will be generated along the gradient direction (Fig. 3b) [31].

Nevertheless, such an effect is usually negligible for most dielectric materials due to the low flexoelectric coefficient (f), which is of the order of e/a (or 10^{-11} - 10^{-10} C/m), where e is the electronic charge and a is the lattice parameter. f is also related to the dielectric susceptibility χ as $f=\gamma\chi(e/a)$, where γ is a material related constant [32]. This relation suggests that high dielectric permittivity materials could possibly exhibit high flexoelectric effect [33,34].

Following this prediction, Ma and Cross determined the flexoelectric coefficients of perovskite ferroelectric materials, including lead magnesium niobate (PMN) [35,36], barium strontium titanate (BST) [37], lead zirconate titanate (PZT) [38,39], and BaTiO₃ [40]. These materials exhibited much higher f values at the level of 10^6 C/m owing to their large permittivities (3000-11000). The constants γ are also related to the chemistry of materials due to the different ionic bonding strength. The Ba-based perovskites showed much higher γ values ($\gamma_{\text{BST}}\sim 9.3$, $\gamma_{\text{BaTiO}_3}\sim 12$); while the γ value of other perovskites were below one ($\gamma_{\text{PMN}}\sim 0.65$, $\gamma_{\text{PZT}}\sim 0.57$). These results indicated that Ba-based perovskites could be better candidates if the flexoelectric effect is of major interest.

When the lattice size is only an order of magnitude or two smaller than the width of the beam, as is in the case of a NW, the strain gradient and the resulting flexoelectric effect would become significant [41,42]. For nanosized piezoelectric materials, the piezoelectricity would be further enhanced by the appreciable flexoelectricity. The mathematic framework presented by Majdoub et al. predicted the size-dependent flexoelectric enhancement on the piezoelectricity of ferroelectric nanostructures [18]. A non-linear increase of the effective piezoelectric coefficient (d_{eff}) was suggested when the beam thickness decreases. Using the flexoelectric coefficients estimated from *ab initio* calculations [43] (5.46 nC/m), a more than 400% enhancement on the effective piezoelectric coefficient (the overall measure of the electromechanical coupling considering both piezoelectric and flexoelectric effects) was predicted on tetragonal BaTiO₃ beam when the thickness was below 1 μm [44]. The same group also estimated the energy harvesting capability of ferroelectric beams when the flexoelectric effect was considered [45]. Due to the electromechanical coupling effect, the beam bending rigidity will increase with the enhancement of polarization. This is reflected by the increasing of "effective coupling coefficient" (ζ_{eff}). Compared to the known value of PZT beam harvester [46], the harvested power was expected to show a 50-100% improvement when the beam thickness is below 50 nm in the short circuit resonance mode.

Characterization of piezoelectric potential from piezoelectric NWs

Contact AFM scanning approach

The first detection of strain-induced potential from piezoelectric NWs was performed by AFM on vertically aligned ZnO NW arrays [47]. The ZnO NWs were grown on GaN

substrate and connected through a silver bottom electrode (Fig. 4a). A conductive AFM tip (Si coated with Pt) was used to create deformation of the vertical NWs and collect electrical signal simultaneously. Through a contact mode, the AFM tip scanned across the NW tips and bent the NWs laterally, as shown in Fig. 4b. Bending of the ZnO NW created positive potential on the stretching side and negative potential on the compressive side. Because the metal-semiconductor contact between the Pt-coated AFM tip and the ZnO NW is a Schottky-type contact, only when the semiconductor side has lower potential than the metal side, a forward-biased connection is formed, thus free charges can flow through and neutralize the piezoelectric potential. Little charge flow is allowed when the ZnO side exhibits higher potential than the metal side (the reversely biased connection), which is the condition when the AFM pushes the stretching side of the NW. Under this situation, piezoelectric energy would accumulate inside the NW, and then be partially released in a pulsed form when the AFM tip touches the other side. This condition can be considered as integrating a regular piezoelectric beam with a diode together into one system.

The Schottky contact between the Pt surface and ZnO NW gives unipolar electrical output pulses when the AFM tip scans a ZnO NW array, as shown in Fig. 4c. The output potential was measured on an external load of resistance $R_L=500\text{ M}\Omega$ and most peaks were identified as $\sim 6\text{--}9\text{ mV}$.

Similar experiments have also been conducted on larger sized single ZnO wire, and $\sim 10\text{ mV}$ potential outputs were detected each time when the Pt-coated AFM tip bent the wire and scanned across the wire and reached the other negatively charged side [48]. Tens of mV output was typically observed from ZnO NWs, although the theoretical prediction has suggested a much higher potential output. The big discrepancy can be associated with the contact issue between the AFM tip and the NW surface, as well as the relatively high intrinsic doping concentration of ZnO synthesized in regular vapor-based growth processes.

Three dimensional Kelvin probe microscopy (3DKPM) approach

Surface potential can also be measured in a non-contact way by scanning Kelvin probe microscopy (SKPM). However, a general class of measurement errors is always introduced by sample-topographical effects, especially the strong dependence of the measured surface potential on distance between the AFM tip and sample, thus it is not able to provide reliable characterization on NWs due to the large topography variation. Recently, Bayerl and Wang devised a new 3DKPM technique to transcend the limitations of SKPM and enable quantitative surface potential mapping of high topography surfaces [49].

3DKPM entails scanning an AFM probe configured for non-contact SKPM operation. The probe is sequentially moved to

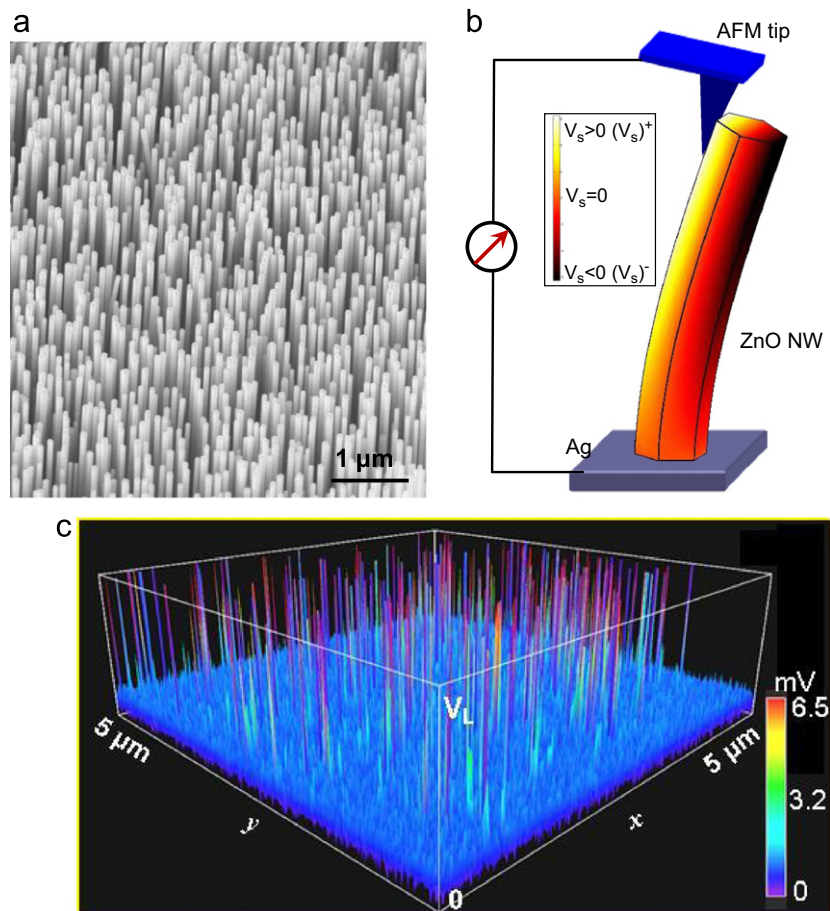


Figure 4 (a) Vertically aligned ZnO NW arrays. (b) Schematic diagram showing the AFM-based measurement of the bending-induced piezoelectric potential on ZnO NWs. (c) Electric signal collected by AFM on a ZnO NW array [47].

each designed testing position where it is lifted to a uniform height above the surface and slowly lowered until the probe achieves contact with the surface (Fig. 5a). The potential recorded during the approaching corresponds to the potential distribution in the column of space above each testing position. Such spatially resolved potential data can then be reconstructed into a 3D image throughout a volumetric scan. Fig. 5b shows the spatial potential distribution in a plane bisecting a single pair of Au electrodes (left one grounded and right one biased by 100 mV), which is qualitatively identical to the finite element simulation (not considering the potential scaling factor) evidencing the accurate spatial potential mapping capability of 3DKPM. The surface potential identified from the electrode surface scaled linearly with the applied bias (Fig. 5c) showing that the 3DKPM technique can accurately quantify the potential of charged surfaces. 3DKPM can accurately map the electric potential in a 3D space with an electric potential gradient resolution of at least 5 mV per 50 nm.

With the capability for high-resolution surface potential quantification established, 3DKPM was applied to characterizing the piezoelectric potential of ZnO NWs. Spatial potential mapping was obtained on a ZnO NW when it was bent and straight. Asymmetry in the potential distribution between the

left (compressed) and right (stretched) sides is apparent near the surface of the bent NW (Fig. 6a); while the straight NW gave a fairly symmetric potential distribution (Fig. 6b). By extracting the potential difference on the two side surfaces, the piezoelectric potential was identified to be ~ 400 -600 mV from different bending conditions (Fig. 6c), which matches well with theoretical calculations [19]. 3DKPM methods therefore have the potential to become an invaluable tool for ongoing characterization of size-enhanced piezoelectric polarization effects in piezoelectric micro/nanostructures of high topography and low dimension.

MEMS-based approaches

MEMS-based devices have also been developed for characterizing the piezoelectric potential of NWs. By integrating a BaTiO₃ NW with a mobile base that can provide a precise linear motion (resolution < 1 nm), the piezoelectric responses were determined under axial strains [50]. The maximum piezoelectric potential was found to be ~ 25 mV and the output potential was linearly related to the driving amplitude. Such output voltage amplitude was comparable to those determined from ZnO NW, although the piezoelectric

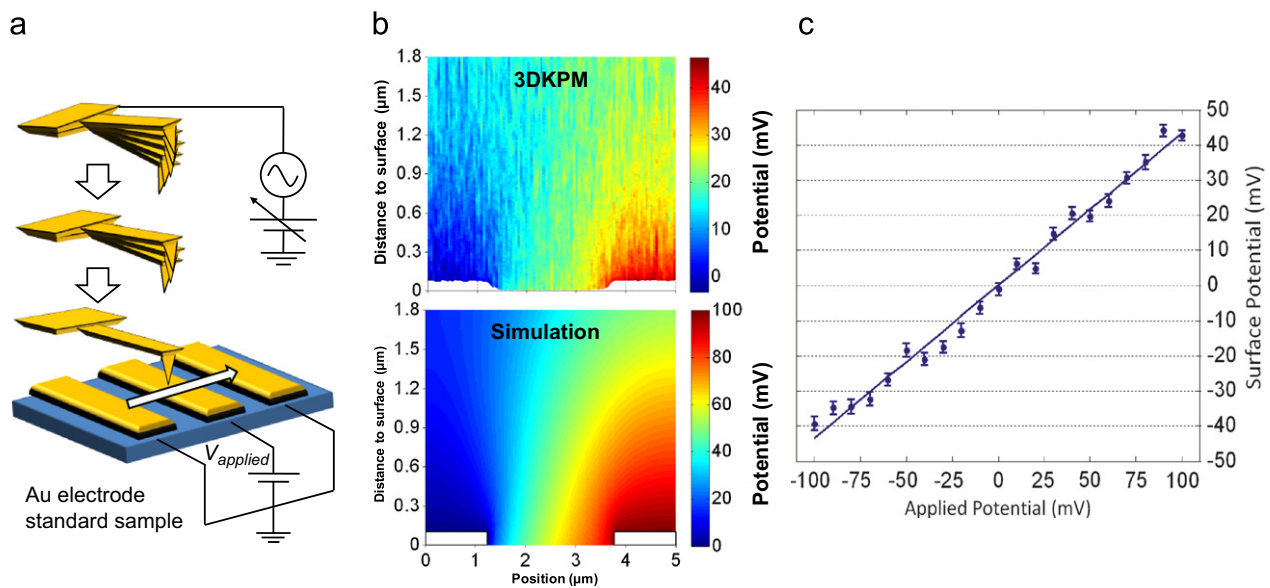


Figure 5 (a) Schematic of the 3DKPM approach. (b) 3DKPM measured and simulated potential distribution above a pair of electrodes. (c) Plot of measured potential versus applied potential.

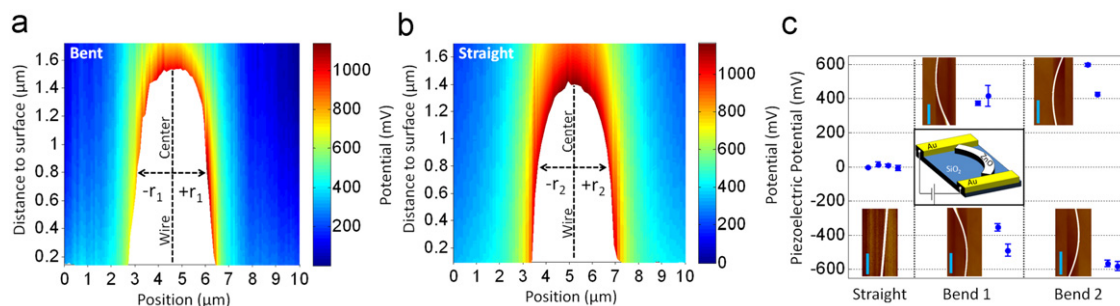


Figure 6 3DKPM potential maps of (a) bent and (b) straight ZnO NW. (c) Piezoelectric potential quantification of ZnO NWs with multiple bending configurations (insets).

coefficient of BaTiO₃ is higher. As discussed earlier, this is due to the higher dielectric constant of BaTiO₃. From the number of charge produced by the BaTiO₃ NW, the output electrical energy per straining cycle was calculated to be ~ 0.3 aJ at driving amplitude of 5 V.

A bridge-type device was made by placing a poly(vinylidene fluoride) (PVDF) fiber across a pair of electrode on a flat flexible substrate [51]. The voltage and current signal was measured from the PVDF nanofiber by stretching and releasing the flexible substrate at a constant rate (2 Hz). The typical voltage was measured to be ~ 5 -30 mV and current was ~ 0.5 -3 nA. Integrating the product of voltage and current with respect to time gives the overall electric energy output. Comparing this energy to the input mechanical energy that was needed to create the strain, the energy conversion efficiency was estimated to be as high as 21.8%. Such a value is much higher than those can be achieved by PVDF thin films (typically 0.5-4%). It was suggested that the higher energy conversion efficient of PVDF nanofibers was due to the much smaller domain wall motion barrier in PVDF nanofibers (ca. 0.01% strain) compared to that of PVDF thin films (ca. 0.3% strain). Thus, higher polarization could be produced by the nanofibers under the same strain.

Prototypes of piezoelectric NGs

The discovery of appreciable piezoelectricity from ZnO NWs has led to the development of a series of NW-based piezoelectric NGs. Most recent models have showed the capability of powering small electronic devices. Representative models of piezoelectric NGs will be reviewed in this section.

Ultrasonic wave-driven NGs—the first prototype

Integrating a Pt coated serrated electrode with vertically aligned ZnO NWs created the first NG prototype that converted ultrasonic waves into electricity [14]. As schematically shown in Fig. 7a, an array of aligned ZnO NWs was covered by a serrated Si electrode coated with Pt. The Pt coating not only enhanced the conductivity of the electrode, but also created a Schottky contact at the interface with ZnO. The NWs were grown on GaN substrates and the top electrode was composed of parallel serrated trenches fabricated on a (0 0 1) orientated Si wafer and coated with a thin layer of Pt. A cross-sectional image of a packaged NG is shown in Fig. 7b. Some NWs were in direct contact with the top electrode, but some were located between the teeth of the electrode. Under the application of ultrasonic waves, the top electrode would move downward and push the NW leading to a lateral bending. The bending-induced piezoelectric potential would then be collected by the Pt film when the Schottky junction between the NW and Pt electrode was forward biased.

Due to the *in situ* rectifying effect of the Schottky contact, the detected output electric signal exhibited a direct current (DC) characteristic. Although each NW would still produce electric pulses, accumulation of the output from all NW generated a constant DC current signal with large noises, as shown in Fig. 7c. The polarization of the DC signal was consistent with the bias direction of the Pt-ZnO

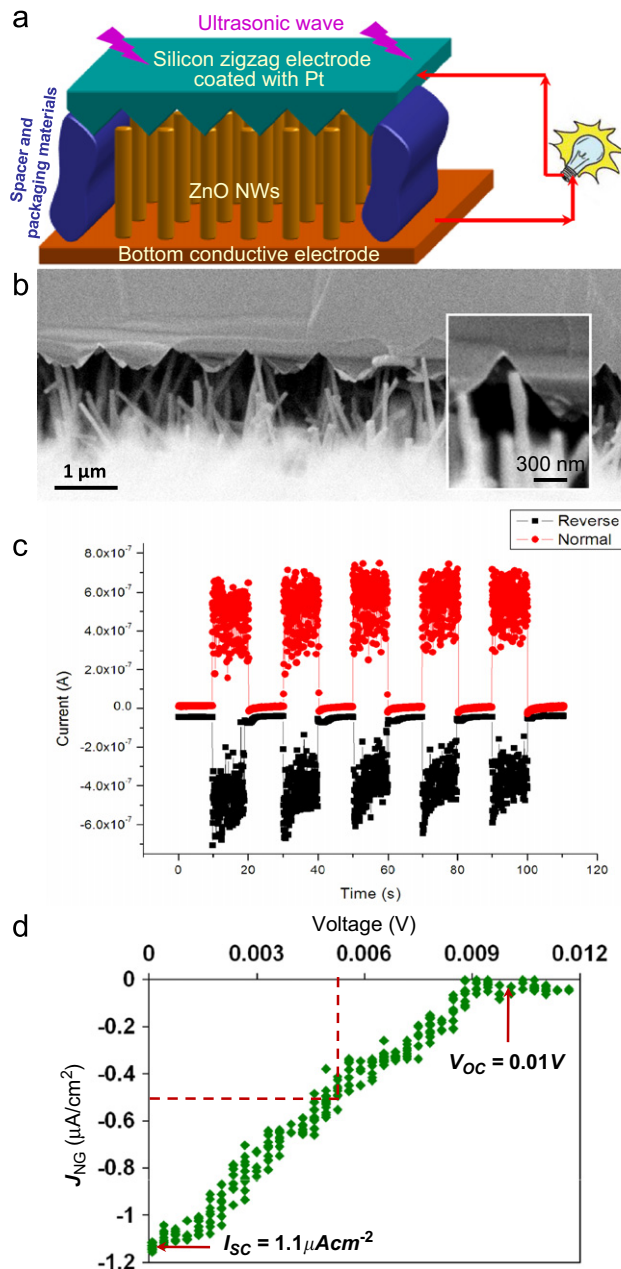


Figure 7 ZnO NW-based piezoelectric NGs. (a) Schematic diagram showing the design and structure of the NG. (b) Cross-section of the NG showing the integration of aligned NWs and the top electrode. Inset shows a NW that is forced by the electrode to bend [14]. (c) A typical DC current output of an ultrasonic-driven NG [52]. (d) J - V curve of the NG during normal operation, where the short-circuit current and open-circuit voltage can be identified [53].

Schottky barrier. When the connection of electrical measurement system was switched between the two electrodes of the NG, the polarization of the output signal would be reversed accordingly but the signal amplitude was unaffected, as shown by the black curve in Fig. 7c [52]. This phenomenon further proved the Schottky effect to the NG output and it is considered as a necessary condition to distinguish valid signals from artifacts.

The DC output of ultrasonic wave-driven NGs allows the performance characterization by connecting a variable DC voltage source as the load, which is a condition similar to that of solar cell characterization. A typical J - V curve of a NG is shown in Fig. 7d demonstrating an open circuit voltage of ~ 10 mV and a short circuit current density of $\sim 1 \mu\text{A}/\text{cm}^2$, which suggested an optimum output power of ~ 10 nW/ cm^2 . From the shape of the curve, the fill factor (FF) was determined to be $\sim 25\%$. Thus the operational power of that particular NG was ~ 2.5 nW/ cm^2 [53]. The low FF was likely associated with the large internal resistance due to a large number of branching NW and the poor contact between NWs and the Pt electrode. In an ideal case, if each NW were involved in the energy conversion process, the output power would be raised to the $\mu\text{W}/\text{cm}^2$ level or higher [54].

Power fibers

In addition to the ultrasonic wave driven NG, a textile fiber based NG has been developed for harvesting low-frequency vibration/friction energies [55]. The fibers used in the fabrication were Kevlar 129 fibers, on which ZnO NWs were grown radially (Fig. 8a). Along the entire length of the fiber, ZnO NWs exhibited a very uniform coverage and well preserved cylindrical shape (Fig. 8b). The spaces between the NWs are large enough for them to be bent to generate the piezoelectric potential.

A double-fiber system was designed to demonstrate the capability of harvesting mechanical energy. As shown in Fig. 8c, two fibers, one coated with a 300-nm-thick gold layer and the other as-grown, were entangled to form the core for power generation. Once the two fibers were firmly entangled together, some of the gold-coated NWs penetrated slightly into the spaces between the uncoated

nanowires rooted at the other fiber. Thus, when there was a relative sliding/deflection between them, the bending of the uncoated ZnO NWs produced a piezoelectric potential across their width, and the Au-coated NWs acted as the electrode for collecting and transporting the charges.

The performance of the fiber NGs was characterized by measuring the short-circuit current (I_{sc}) and open-circuit voltage (V_{oc}) when the gold-coated fiber was pulled and released at a controlled frequency. ~ 5 pA current pulses were detected at each pulling-releasing cycle (blue curve in Fig. 8d). Negative current pulses with the same amplitude were received (pink curve in Fig. 8d) when the current meter was reverse-connected. The small output current is attributed mainly to the large loss in the fiber due to an extremely large inner resistance ($R_i \approx 250$ M Ω). The open-circuit voltage was measured to be ~ 1 -3 mV from the same fiber NG. The piezoelectric output can be enlarged by integrating multiple fibers together. In a small yarn containing 6 fibers (three covered with Au-coated NWs, and three covered with untreated ZnO NWs), an average current of ~ 0.2 nA was achieved, which was ~ 30 -50 times larger than the output signal from a double-fiber NG. This is due to the enhanced surface contact area among those fibers. Reducing the inner resistance of the fiber and the NWs was also found effective for enhancing the output current. By depositing a conductive layer directly onto the fiber before growing the ZnO NWs, the output current I_{sc} of a double-fiber NG was increased from ~ 4 pA to ~ 4 nA. I_{sc} was approximately inversely proportional to the inner resistance of the NG. Based on the current and voltage data received, calculation showed that weaving a large number of such fibers together would bring the output power up to ~ 4 -16 mW/ m^2 if the consumption from the device resistance and capacitance were neglected.

Prediction of the power output from piezoelectric NWs

The first independently operated NG prototype was designed to be driven by ultrasonic waves. In fact, stimulating a piezoelectric beam into vibration has been broadly used for harvesting mechanical energy in most MEMS devices. Therefore, to quantitatively understand the dynamic responses of a piezoelectric NW under vibration is essential for the development of NGs. The system used for dynamic analysis is schematically shown in Fig. 9a. The nanostructure was assumed to have its bottom end fixed on the substrate and the other end to be free. An external mechanical energy in a wave form is applied through the substrate and agitates the vibration of the NW at the same frequency. The external mechanical energy is also assumed to be continuous, constant and sufficiently large. Such vibrations will induce alternating electrical charges along the two side surfaces of the NW.

Considering each NW as a single degree-of-freedom (DOF) system and using the strain-potential relationship derived for a bending NW, the power and efficiency were calculated at different lengths and thicknesses by assuming that the NWs are agitated into oscillation at their resonant frequencies with a fixed mechanical damping ratio of 0.005 [21]. The plots of these relationships for ZnO and BaTiO₃ NWs are shown in Figs. 9b and c, respectively. Two general conclu-

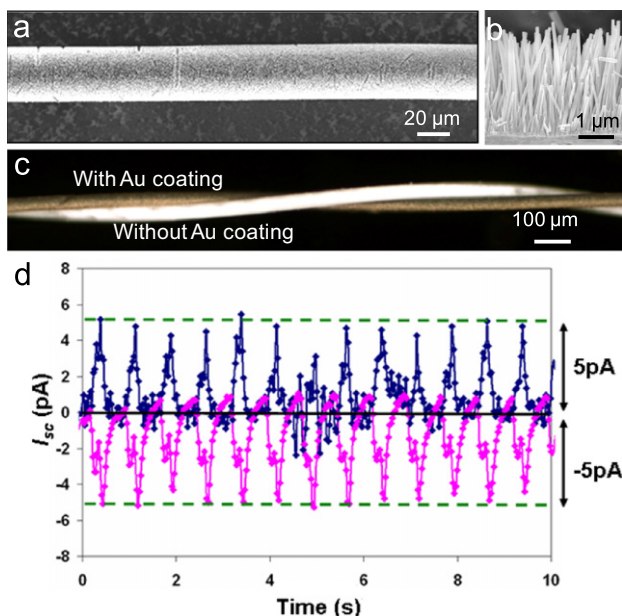


Figure 8 ZnO NW-based fiber NGs. (a) A Kevlar fiber uniformly coated with ZnO NW arrays. (b) A cross-section image of the fiber. (c) Optical image of the NG fabricated by two ZnO NW-coated fibers, one with gold coating and one without. (d) The current output measured from a double-fiber NG [55].

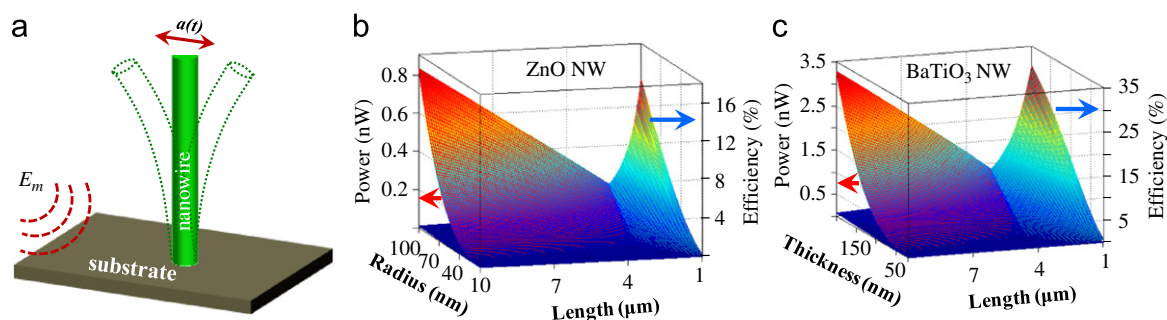


Figure 9 (a) Schematic of a dynamic analysis model, where the NW is agitated into vibration by an external vibration mechanical energy applied through the substrate. The output power and energy conversion efficiency of (b) ZnO and (c) BaTiO₃ NWs at their resonant frequencies as functions of their length and thickness [21].

sions can be drawn from the plots regardless of the morphology and material. First, the output power increases with the increasing of the nanostructures' volume. This agrees with the property of regular piezoelectric bulk materials—more volume brings more piezoelectric power. Second, the energy conversion efficiency at the resonant frequency increases rapidly with the reducing of the nanostructure's aspect ratio. This suggests that high energy conversion efficiency would be found in a thin-film-like morphology, which is resulted from the faster decay of the mechanical damping energy compared to the electric output energy when the aspect ratio decreases. The different tracks of the output energy and efficiency indicate the existence of an optimal size range, where the NWs will output a reasonably high power with a reasonably good efficiency. Such a size range can be identified from the plots where the power surface intersects with the efficiency surface. For BaTiO₃ NWs, their lengths should be 4–5 μm and width should be larger than 100 nm. For ZnO NWs, their lengths should be 3–4 μm and side widths should be larger than 50 nm. It should be noted that these predictions were established based on the assumption that the ambient mechanical energy is always sufficient. Although the plots show a continuous increasing tendency of both the power and efficiency with the increase of radius or thickness, too large size would need a significantly high external mechanical energy to drive the vibration. Under this condition, the assumption of unlimited mechanical energy will not apply and the solution is beyond the capability of this method.

Piezoelectric polymer microbelts for harvesting energy from respiration

It has been clearly shown that increasing the number of NWs while maintaining the optimal geometry could substantially improve the output power. In addition to the vertical NW arrays that were used in the first NG prototypes, laterally aligning NWs are considered as a good strategy for effectively integrating a large number of NW over a large area, thus improve the output of NGs. Many current designs of NGs have such a lateral film-type configuration, which raised the output electric energy to the μW level [56–59]. The capability of powering small electronic devices has also been successfully demonstrated [58,60–63].

As we briefly discussed in Section 2.3, PVDF is a piezoelectric polymer that shows good promises for the develop-

ment of NGs. Its polymeric nature allows it to be easily fabricated into a 2D film morphology with a good potential for scaling up. Sun et al. recently demonstrated an application of PVDF thin films for harvesting energy from low-speed air flow as well as from simulated human respiration—an important biological energy source for powering implantable electronic devices [64].

The design for characterizing the capability of harvesting energy from air flow is schematically shown in the inset of Fig. 10a. A PVDF microbelt (20 mm \times 2 mm \times 26 μm) was tightly suspended across the front edge of a trench which was \sim 1 cm deep. The air flow was provided by a nozzle placed \sim 3 cm in front of the trench and the flow speed was measured at the position where the microbelt was located. Direct measurement of the voltage difference between the top and bottom electrodes of the PVDF microbelt demonstrated that appreciable piezoelectric potential was produced by low-speed air flow. Fig. 10a shows the open-circuit voltage (V_{OC}) of the PVDF microbelt as a function of air flow speed. Peak V_{OC} of \sim \pm 6 V was detected at an air flow speed of 5 m/s. The voltage amplitude monotonically decreased following the reduction of air flow speed. At the air flow speed of \sim 1 m/s, the output voltage dropped to less than 0.1 V due to the very small oscillation amplitude.

By connecting the PVDF microbelt to a capacitor (1 mF) through a bridge circuit, a practical power source was demonstrated. Based on the saturation voltage that can be eventually maintained on the capacitor under different air flow speeds, the usable energy stored in the capacitor from microbelt oscillation was determined as a function of the air flow speed (Fig. 10b). The maximum stored energy increased from \sim 8 μJ at 2 m/s to 1.8 mJ at 4 m/s. This energy level is sufficient to power small electronic devices, which was demonstrated using a digital stopwatch. As shown in the inset of Fig. 10b, the stopwatch was connected as a load on the capacitor. By applying constant air flow at a speed of 3.5 m/s, the stopwatch was operated normally. Sustained production of useful-level electrical power by PVDF microbelts under low-speed air flow was thus demonstrated. Reducing the thickness of the microbelts allows this device to harvest energy from even lower air flow speeds ($<$ 1 m/s).

The small size of PVDF microbelts and their capability of producing μW -level power under low-speed air flow make feasible harnessing energy from respiratory processes. A typical respiration air flow rate follows a sine curve with a peak rate of \sim 0.4 l/s (corresponding to \sim 2 m/s considering

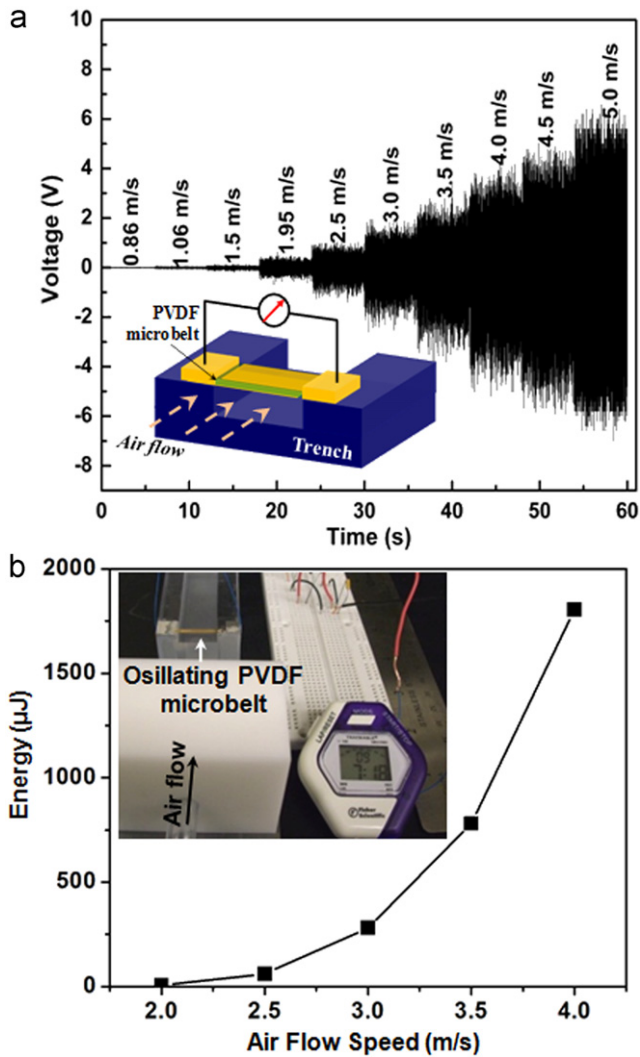


Figure 10 (a) Open-circuit voltage measured under different air flow speed. Inset is the schematic design of a PVDF microbelt for harvesting energy from air flow. (b) Energy stored by the capacitor under different wind speeds. Inset shows an operating stopwatch powered by a microbelt under air flow speed of ~ 3.5 m/s.

the average area of adult human nostrils) and a periodicity of ~ 5 -6 s [65]. Certainly, lower cut-in speed would allow more energy to be harvested by a microbelt. A $17\ \mu\text{m}$ -thick PVDF microbelt was used for fabricating such a device. The microbelt was fixed at the center of a cylindrical channel with a cross section area of $\sim 1\ \text{cm}^2$. One end of the channel was connected to a compressible plastic chamber that simulated the function of a lung and the other end was open (Fig. 11a). The plastic chamber was squeezed and released every 6 s producing air flow in and out through the tunnel with a peak rate of ~ 2.3 m/s (Fig. 11b, calculated from the volume change of the plastic chamber per unit time ~ 0.23 l/s). This operation provided a close simulation of typical adult's respiration.

Resonant oscillation of the microbelt was stimulated by the air flow through the channel and its V_{OC} output was continuously monitored. The voltage output was clearly correlated to the instantaneous flow rate and peak voltage output of ~ 0.4 - 0.5 V was detected at the highest “exhalation”

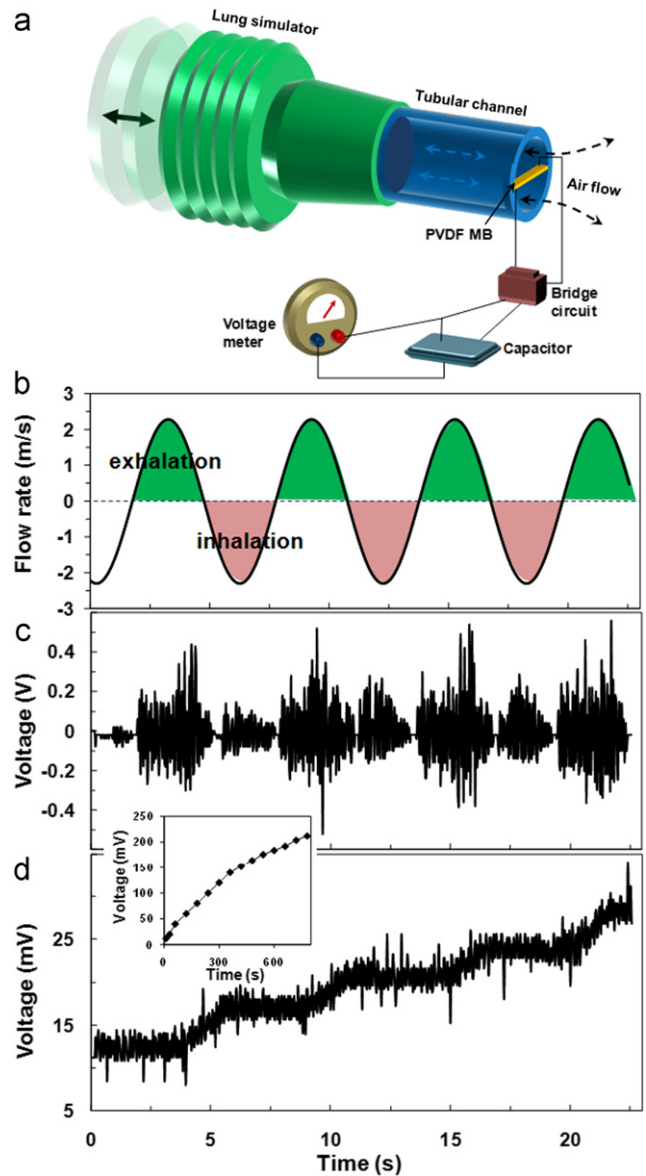


Figure 11 Energy harvesting from simulated respiration by PVDF microbelts. (a) Schematic design for simulated respiration energy harvesting. (b) Air flow rate through a tubular channel with a matching pattern to the normal respiration of an adult. (c) Corresponding V_{OC} measured on a PVDF microbelt fixed at one end of the tubular channel. (d) Voltage increase on a capacitor that was connected to the PVDF microbelt through a bridge circuit. Inset is the long-time voltage increase trend on the capacitor.

flow rate of ~ 0.5 l/s (Fig. 11c). Lower output voltage was observed during “inhalation” cycles. This was likely due to asymmetry of the air flow profile between inhalation and exhalation. In order to demonstrate the feasibility of converting energy from respiration to useful electricity, a 1 mF capacitor was connected to the microbelt through a bridge circuit and the increasing voltage curve is shown in Fig. 11d. It reveals that one respiration cycle could increase the capacitor voltage by ~ 5 mV. A majority of voltage increase was registered with the “exhalation” cycles owing to the higher voltage output of the microbelt. A continuous

12 minutes of simulated respiration produced a capacitor voltage output of ~ 200 mV, corresponding to $20 \mu\text{J}$ of electrical energy storage. This experiment showed that microbelts made from PVDF can oscillate under low-speed air flow and generate electrical energy sufficient for powering small electronic devices. This capability is ideal for harvesting energy from respiration, and thus has the potential for powering implantable biomedical devices.

Challenges and opportunities

Using piezoelectric nanomaterials for harvesting mechanical energy in the micro- or nano-scale is a very promising concept for realizing self-powered nanoelectronics. To date, various designs and piezoelectric nanomaterials have been applied to NGs. In order to pave the road toward integratable NGs for nanoelectronics, the essential goal is to improve the power density and energy conversion efficiency thus to shrink the device size down to the micrometer level while maintaining a reasonably high output power. Despite current research efforts on material processing and NG design optimizing, there are several fundamental aspects that must be addressed.

First, piezoelectric effect at the nanometer scale: The piezoelectric nanomaterials used in current NGs are mostly in the size range of > 100 nm. Therefore, their piezoelectric properties are basically the same as their bulk form. Theoretical predictions have shown that within the nanometer regime, flexoelectric effect may play a significant role and enhance the electromechanical coupling. Currently, experiment-based analysis of the piezoelectric and flexoelectric properties at the nanometer scale is very limited. Fundamental understandings of the piezoelectric, ferroelectric, and flexoelectric effects on single-crystalline NWs is of great importance for predicting the piezoelectric potential, quantifying the mechanical-to-electric energy conversion efficiency, and optimizing the size selection of different types of nanomaterials.

Second, mechanical property at the nanometer scale: Number of research has been conducted to reveal the mechanical property (the Young's modulus and critical strain) of ceramic materials at the nanometer scale. Largely enhanced fracture strain was observed on the NW morphologies [22,66-68]. In order to optimize the material selection, a systematic understanding of the mechanical properties as a function of the dimensions of different piezoelectric materials is necessary. Specifically, for NWs with their sizes < 100 nm, rectification might be needed for re-defining the elastic constant matrix. With this information, the mechanical energy that is necessary to create certain level of strain can be quantified thereby the corresponding energy conversion efficiency.

Third, coupling between the piezoelectric and semiconductor properties (the piezotronic effect): Most piezoelectric materials are actually semiconductors as well. They can be doped intrinsically or extrinsically to show appreciable free charge concentration. The piezoelectric effect would interact with the charge transportation and induce new phenomena or operation principles. For example, the Schottky barrier formed between ZnO and metal electrodes can in situ rectify the potential output [47]. The conductivity of a ZnO NW can be regulated by the appearance of

piezoelectric potential [69]. Understanding of how electron distribution and semiconductor band structures are interacted with piezoelectric potential would offer new insights on the capability of mechanical energy harvesting.

Last, fabrication and manufacturing: In addition to above scientific issues, the engineering challenges are mostly lying on the piezoelectric nanomaterial fabrication and device integration. Designing a NG system that can be adapted to large-scale roll-to-roll processing would substantially reduce the fabrication cost and eventually lead this exciting concept toward a practical nanoscale power source.

Conclusion

This paper reviews the development of NGs from the fundamental principles to theoretical predictions to practical devices. Compared to conventional piezoelectric material-based mechanical energy harvesters, using NWs would potentially improve the energy conversion efficiency, enhance the sensitivity to low-level mechanical energy sources, and extend the device lifetime. ZnO NW is the first nanomaterial that has been applied for NG development. Leading by the research on ZnO NWs, NWs made from other piezoelectric materials, including BaTiO₃, PZT, and PVDF were also studied to reveal their mechanical energy conversion capability. Different designs of NG were implemented mostly based on ZnO NW arrays. Integration of a large number of ZnO NWs was demonstrated as an effective pathway for improving the output power. The power output from NGs is already sufficient to support the operation of small electronic devices, such as LEDs, LCDs and NW-based sensors. Addressing several fundamental scientific issues, including the nanometer-scale piezoelectric and mechanical properties and the piezotronic effect would substantially enrich our knowledge of NG designing and operation principles. Combination of in-depth scientific understanding and advanced engineering fabrication approaches would eventually lead the promising NG concept to a practical power source for the realization of self-powered nanoelectronic devices.

Acknowledgment

We thank C. Sun, J. Shi, and D. Bayerl for their contributions to the work reviewed in this article. We also thank the financial support from National Science Foundation under grant Nos. DMR-0905914 and CMMI-0926245, DARPA under grant No. N66001-11-1-4139, and UW-Madison graduate school.

References

- [1] R. Shad, S.L. Eli, B. Jessy, C. Eric, R. Elizabeth, L. Elaine, O. Brian, M.R. Jan, V. Sundararajan, K.W. Paul, IEEE Pervasive Computing 4 (2005) 28-36.
- [2] S. Roundy, P.K. Wright, J. Rabaey, A study of low level vibrations as a power source for wireless sensor nodes, Computer Communications 26 (2003) 1131-1144.
- [3] J.A. Paradiso, T. Starner, IEEE 4 (2005) 18-27.
- [4] J.M. Donelan, Q. Li, V. Naing, J.A. Hoffer, D.J. Weber, A.D. Kuo, Science 319 (2008) 807-810.
- [5] G.K. Ottman, H.F. Hofmann, A.C. Bhatt, G.A. Lesieutre, IEEE Transactions on Power Electronics 17 (2002) 669-676.

- [6] G. Jonathan, J. Feenstra, H.A. Sodano, K. Farinholt, *Smart Materials and Structures* 16 (2007) 1810.
- [7] S. Priya, *Journal of Electroceramics* 19 (2007) 167-184.
- [8] A.P. Chandrakasan, N. Verma, D.C. Daly, *Annual Review of Biomedical Engineering* 10 (2008) 247-274.
- [9] H.A. Sodano, D.J. Inman, G. Park, *The Shock and Vibration Digest* 36 (2004) 197-205.
- [10] S. Meninger, J.O. Mur-Miranda, R. Amirtharajah, A. Chandrakasan, J.H. Lang, *IEEE Transactions on Very Large Scale Integration (VLSI) Systems* 9 (2001) 64-74.
- [11] C.B. Williams, R.B. Yates, *Sensors and Actuators A: Physical* 52 (1996) 8-11.
- [12] G.M. Whitesides, G.W. Crabtree, *Science* 315 (2007) 796-798.
- [13] V.S. Arunachalam, E.L. Fleischer, *MRS Bulletin* 33 (2008) 264-276.
- [14] X.D. Wang, J.H. Song, J. Liu, Z.L. Wang, *Science* 316 (2007) 102-105.
- [15] Z.L. Wang, *Scientific American* 298 (2008) 82-87.
- [16] Z.L. Wang, *Advanced Functional Materials* 18 (2008) 3553-3567.
- [17] R. Yang, Y. Qin, C. Li, G. Zhu, Z.L. Wang, *Nano Letters* 9 (2009) 1201-1205.
- [18] M.S. Majdoub, P. Sharma, T. Cagin, *Physical Review B* 77 (2008).
- [19] Y. Gao, Z.L. Wang, *Nano Letters* 7 (2007) 2499-2505.
- [20] Y. Gao, Z.L. Wang, *Nano Letters* 9 (2009) 1103-1110.
- [21] C. Sun, J. Shi, X. Wang, *J. Appl. Phys.* 108 (2010) 034309-034311.
- [22] S. Hoffmann, F. Ostlund, J. Michler, H.J. Fan, M. Zacharias, S.H. Christiansen, C. Ballif, *Nanotechnology* 18 (2007) 205503.
- [23] V.S. Mashkevich, K.B. Tolpygo, *Soviet Physics JETP* 5 (1957) 435-439.
- [24] K.B. Tolpygo, *Soviet Physics Solid State* 4 (1963) 1297-1305.
- [25] S.L. Kogan, *Soviet Physics Solid State* 5 (1964) 2069-2070.
- [26] E.V. Bursian, N.N. Tranov, *Soviet Physics Solid State* 16 (1974) 760-762.
- [27] R. Maranganti, N.D. Sharma, P. Sharma, *Physical Review B* 74 (2006) 014110.
- [28] R.B. Meyer, *Physical Review Letters* 22 (1969) 918.
- [29] M. Marvan, A. Havránek, *Progress in Colloid Polymer Science* 78 (1988) 33-36.
- [30] R. Lakes, *IEEE Transactions in Biomedical Engineering* BME-27 (1980) 282-283.
- [31] E.V. Bursian, O.I. Zaikovskii, *Soviet Physics Solid State* 10 (1968) 1121-1124.
- [32] A.K. Tagantsev, *Soviet Physics JETP* 61 (1985) 1246-1254.
- [33] A.K. Tagantsev, *Phase Transitions* 35 (1991) 119-203.
- [34] M. Marvan, A. Havrdnek, *Solid State Communications* 101 (1997) 493-496.
- [35] W. Ma, L.E. Cross, *Applied Physics Letters* 78 (2001) 2920-2921.
- [36] W. Ma, L.E. Cross, *Applied Physics Letters* 79 (2001) 4420-4422.
- [37] W. Ma, L.E. Cross, *Applied Physics Letters* 81 (2002) 3440-3442.
- [38] W. Ma, L.E. Cross, *Applied Physics Letters* 82 (2003) 3293-3295.
- [39] W. Ma, L.E. Cross, *Applied Physics Letters*. 86 (2005) 072903-072905.
- [40] W. Ma, L.E. Cross, *Applied Physics Letters*. 88 (2006) 232902-232903.
- [41] C.L. Bauera, W.A. Brantley, *Material Science and Engineering A* 5 (1970) 295-297.
- [42] J. Fousek, L.E. Cross, D.B. Litvin, *Materials Letters* 39 (1999) 287-291.
- [43] R. Maranganti, P. Sharma, *Physical Review B* 80 (2009) 054109.
- [44] M.S. Majdoub, P. Sharma, Ccedil, T. Agbrevein, *Physical Review B* 77 (2008) 125424;
M.S. Majdoub, P. Sharma, Ccedil, T. Agbrevein, *Physical Review B* 79 (2009) 119904.
- [45] M.S. Majdoub, P. Sharma, T. Cagin, *Physical Review B* 78 (2008) 121407.
- [46] Y.C. Shu, I.C. Lien, *Smart Materials and Structures* 15 (2006) 1499-1512.
- [47] Z.L. Wang, J.H. Song, *Science* 312 (2006) 242-246.
- [48] J.H. Song, J. Zhou, Z.L. Wang, *Nano Letters* 6 (2006) 1656-1662.
- [49] D. Bayerl, X.D. Wang, submitted for publication.
- [50] Z.Y. Wang, J. Hu, A.P. Suryavanshi, K. Yum, M.F. Yu, *Nano Letters* 7 (2007) 2966-2969.
- [51] C. Chang, V.H. Tran, J. Wang, Y.-K. Fuh, L. Lin, *Nano Letters* 10 (2010) 726-731.
- [52] J. Liu, P. Fei, J. Zhou, R. Tummala, Z.L. Wang, *Applied Physics Letters*. 92 (2008).
- [53] C. Xu, X.D. Wang, Z.L. Wang, *Journal of the American Chemical Society* 131 (2009) 5866-5872.
- [54] Z.L. Wang, X.D. Wang, J.H. Song, J. Liu, Y.F. Gao, *IEEE Pervasive Computing* 7 (2008) 49-55.
- [55] Y. Qin, X.D. Wang, Z.L. Wang, *Nature* 451 (2008) 809-813.
- [56] X. Chen, S. Xu, N. Yao, Y. Shi, *Nano Letters* 10 (2010) 2133-2137.
- [57] Y. Qi, M.C. McAlpine, *Energy & Environmental Science* 3 (2010) 1275-1285.
- [58] G. Zhu, R. Yang, S. Wang, Z.L. Wang, *Nano Letters* 10 (2010) 3151-3155.
- [59] R.S. Yang, Y. Qin, L.M. Dai, Z.L. Wang, *Nat. Nanotech* 4 (2009) 34-39.
- [60] S. Xu, Y. Qin, C. Xu, Y. Wei, R. Yang, Z.L. Wang, *Nature Nanotechnology* 5 (2010) 366-373.
- [61] S. Xu, B.J. Hansen, Z.L. Wang, *Nature Communications* 1 (2010) 93.
- [62] M.-Y. Choi, D. Choi, M.-J. Jin, I. Kim, S.-H. Kim, J.-Y. Choi, S.Y. Lee, J.M. Kim, S.-W. Kim, *Advanced Materials* 21 (2009) 2185-2189.
- [63] Y. Hu, Y. Zhang, C. Xu, G. Zhu, Z.L. Wang, *Nano Letters* 10 (2010) 5025-5031.
- [64] C. Sun, J. Shi, D. Bayerl, X.D. Wang, *Energy Environmental Science*, doi:10.1039/C1EE02241E, in press.
- [65] J.K. Gupta, C.-H. Lin, Q. Chen, *Indoor Air* 20 (2010) 31-39.
- [66] M.J. Gordon, T. Baron, F. Dhalluin, P. Gentile, P. Ferret, *Nano Letters* 9 (2009) 525-529.
- [67] A.V. Desai, M.A. Haque, *Sensors and Actuators A: Physical* 134 (2007) 169-176.
- [68] B. Wu, A. Heidelberg, J.J. Boland, *Nature Materials* 4 (2005) 525-529.
- [69] J. Zhou, Y.D. Gu, P. Fei, W.J. Mai, Y.F. Gao, R.S. Yang, G. Bao, Z.L. Wang, *Nano Letters* 8 (2008) 3035-3040.



Dr. Xudong Wang is an assistant professor in the department of Materials Science and Engineering at University of Wisconsin-Madison. His research interests include studying the growth and assembly of oxide nanowire arrays, understanding the coupling effect of semiconductor properties and piezoelectric charge displacement, and developing nanogenerator that uses piezoelectric nanomaterials to convert lowlevel mechanical energy into electricity. He is the recipient of DARPA Young Faculty Award, 3M Non-Tenured Faculty Award, Ross Coffin Purdy Award, Young Innovators Under 35 Award, and KAUST research fellow. He has published 49 papers in peer reviewed scientific journals, contributed 7 book chapters in his research field, and holds 5 patents/provisional patents on oxide nanostructures and nanomaterial-enhanced energy harvesting. His publications have been cited over 3,600 times by peers and his current h-index is 27.